A Proof of Principle for the Phase-Dependent Electrocatalytic Activity of NiTi Shape Memory Alloys for Oxygen Evolution Reaction

Vineetha Vinayakumar[1,2*], Santiago Benito[3*], Aneeta Jose[1], Alexander Kunzmann[4,5], Adarsh Jain[1], Ruben Skjelstad Dragland[7], Mohit Chatwani[1], Blaz Toplak[1], Adithya Aravind[1], Dennis Meier[2,5,6,7], Oluwabi Oluwaseyi[8], Jan Frenzel[8], Sebastian Weber[3], Gabi Schierning[2,4,5], Doris Segets[1,2]

1. Institute for Energy and Materials Processes – Particle Science and Technology (EMPI-PST), University of Duisburg-Essen
2. Center for Nanointegration Duisburg-Essen (CENIDE), University of Duisburg-Essen
3. Institute for Materials, Chair of Materials Technology, Ruhr-Universität Bochum, 44801, Bochum, Germany
4. Institute for Energy and Materials Processes – Applied Quantum Materials, University Duisburg-Essen, Duisburg, Germany
5. Research Center Future Energy Materials and Systems (RC FEMS), Research Alliance Ruhr, Bochum, Germany
6. Faculty of Physics, University of Duisburg-Essen, Lotharstraße 1, D-47057 Duisburg, Germany
7. Department of Materials Science and Engineering, Norwegian University of Science and Technology (NTNU), Trondheim, Norway.
8. Institute for Materials, Chair of Materials Science and Engineering, Ruhr University Bochum, Bochum, Germany

* V. Vinayakumar, vineetha.vinayakumar@uni-due.de, S. Benito, benoito@wtech.rub.de

Abstract

Nickel-titanium (NiTi) shape memory alloys are intermetallic compounds which can exhibit a reversible martensitic phase transformation. While extensively studied for biomedical and actuator applications, their potential as electrocatalysts for the oxygen evolution reaction (OER) remains virtually unexplored. Here, we systematically investigate how phase structure influences OER activity in NiTi alloys by comparing martensite $Ni_{50}Ti_{50}$ (B19' monoclinic) and austenite $Ni_{51.2}Ti_{48.8}$ (B2 cubic). Despite differing by only 1.2 at.% Ni, the investigated specimens exhibit markedly different electrocatalytic behavior. In 1 M KOH containing 15 ppb Fe, the martensitic one requires 40 mV lower overpotential (450 mV vs. 490 mV at 10 mA cm^{-2})

and maintains stable operation at 1.56 V vs. RHE over 12 hours. This improved activity correlates with characteristic phase-dependent properties: enhanced electrical conductivity, finer surface texture, and a markedly increased hydrophilicity of martensite (contact angle 21° vs. 71°). The martensitic phase also shows a 10% larger electrochemically active surface area. Under elevated Fe levels (150 ppb), the martensite phase undergoes stronger surface restructuring and achieves a 370 mV lower overpotential, indicating superior Fe incorporation compared to austenite. Together, these findings demonstrate that the OER performance in NiTi alloys is systematically tunable via their microstructural states and establish phase engineering of intermetallic shape memory alloys as a promising strategy for rationally designing next-generation electrocatalysts for water splitting.

Key words: NiTi shape memory alloys, alkaline water electrolysis, phase engineering, oxygen evolution reaction, microstructure, martensitic transformation

1. Introduction

Nickel-titanium (NiTi) shape memory alloys (SMAs) represent a compelling class of intermetallic compounds that can undergo reversible martensitic transformations between austenitic (B2 cubic, $Pm\bar{3}m$) and martensitic (B19' monoclinic, P21/m) phases [1, 3]. This temperature-dependent, diffusionless transformation occurs within a narrow thermal hysteresis bounded by specific characteristic start and finish temperatures upon cooling (Ms, Mf), and heating (As, Af). Recent comprehensive investigations have revealed significant electronic restructuring during this transformation, including substantial changes in charge carrier density, charge carrier mobility, resistivity, Hall coefficient, and Seebeck coefficient [2, 4-6]. The electronic entropy contribution to the total transformation entropy is considerable for near-equiatomic compositions, with experimental evidence indicating electron redistribution between free electron states (austenite) and bonding states (martensite) [2, 7, 8]. The phase stability and therefore the resulting electronic properties of NiTi SMAs are highly composition-sensitive: deviations from equiatomic compositions toward higher nickel contents stabilize the austenite phase. Mechanistically, this stabilization is driven by the accommodation of excess nickel atoms as anti-site defects, which induce local atomic displacements. These local lattice distortions provide an energetic advantage to the (now imperfect) cubic B2 structure relative to the monoclinic martensite [9]. As a result, each 0.1 at.-% Ni added decreases the temperature Ms at which the transformation starts by approximately 10 K [1] (cf. **Figure S1**). As a result, different compositions exhibit distinct electronic behaviors [4, 5]. Given that the electronic structure influences catalytic activity in electrochemical reactions [10], these documented

electronic modifications suggest that NiTi alloys may represent an unexplored platform for investigating phase-dependent electrocatalytic properties.

Electrochemical water splitting represents a promising pathway for sustainable hydrogen production, yet the oxygen evolution reaction (OER) remains the kinetic bottleneck due to its sluggish kinetics and high overpotentials [11-13]. In alkaline media, earth-abundant transition metals like nickel, cobalt, and iron can be employed; however achieving both high activity and long-term stability remains challenging, with catalysts often exhibiting an inverse relationship between these properties [14-16]. Among these, nickel-based materials have attracted considerable attention as viable OER electrocatalysts in alkaline conditions due to nickel's ability to form electrochemically active oxyhydroxide species under anodic conditions [17, 18]. However, while the intrinsic catalytic potential of nickel is known, how this activity interplays with the complex structural hierarchy inherent to the NiTi system remains an open inquiry. Considering the electronic restructuring described above, specifically the shift between free and bonding electron states, a critical fundamental question emerges, namely to what extent the distinct crystal symmetries and their associated microstructural features, spanning from the crystal lattice to displacive phase transformation interfaces, differentially modulate the oxygen evolution kinetics. Answering this is essential for moving beyond simple compositional tuning to establish precise structure-activity relationships in phase-engineered materials. Intermetallic compounds, characterized by ordered crystal structures and distinct electronic properties from their constituent elements, represent a largely unexplored class of materials for OER electrocatalysis [19-23]. Understanding whether and how alloying modulates their catalytic activity is essential for the rational design of next-generation electrocatalysts and for establishing fundamental structure-activity relationships in multi-metallic systems.

While NiTi SMAs have been extensively studied for biomedical implants [24-26], actuators, and energy harvesting devices [27, 28], their potential as electrocatalytic materials [29], particularly for OER, remains virtually unexplored. The existing literature predominantly addresses the corrosion resistance [30-32] and passive oxide formation of NiTi alloys [33-36] in physiological environments, with no research examining their intrinsic electrochemical activity or intentional application as OER catalysts to the best of our knowledge. This represents a significant knowledge gap, particularly given that NiTi alloys inherently combine two elements: nickel, which serves as the primary catalytic center, and titanium, which is typically present as its oxide, and which mainly acts as a structural and electronic promoter that stabilizes the catalyst and tunes the local environment of the active nickel sites [37-41]. The unique

surface chemistry of NiTi, characterized by dynamic oxide layer formation and phase-dependent restructuring, presents an untapped opportunity to engineer electrocatalytic interfaces with optimized activity and stability.

The electrocatalytic potential of NiTi has been recently demonstrated for the hydrogen evolution reaction (HER), where austenitic NiTi outperformed platinum under alkaline conditions, revealing optimal hydrogen binding energies in the austenite phase [29]. This breakthrough, combined with detailed electronic characterization, suggests that NiTi SMAs represent an untapped class of phase-tunable electrocatalysts. However, the development of strain-engineered catalysts typically relies on complex core-shell structures or elastic substrates, making the intrinsic phase transformation capability of NiTi particularly attractive. Despite the comprehensive characterization of electronic transport properties and recent HER success, the oxygen evolution behavior of bulk NiTi SMAs remains underexplored.

In this work, we present the first comprehensive electrochemical investigation of OER activity in two selected NiTi SMAs representing different phases: $Ni_{50}Ti_{50}$ - martensite and $Ni_{51.2}Ti_{48.8}$ - austenite. Through systematic electrocatalytic performance assessment and microstructural characterizations, we investigate the distinct phase-dependent OER activity in these NiTi intermetallic compounds. The noted superior performance of the martensitic phase over the austenite phase is attributed to synergistic effects arising from enhanced electronic conductivity, increased electrochemical surface area, improved surface wettability, and more favorable Fe incorporation kinetics. Our findings establish a foundation for utilizing the phase-dependent properties of NiTi SMAs to further tune their electrochemical performance in alkaline water electrolysis, opening pathways for future development of phase- and microstructure-engineered intermetallic catalysts for sustainable hydrogen production.

2. Materials and Methods

2.1. Materials and Processing

The alloy compositions selected for this study were chosen to ensure the stability of either the B2 austenite or B19' martensite phase at the testing temperature of 300 K. The dependence of the characteristic transformation temperatures on the nominal nickel content in the $Ni_xTi_{(100-x)}$ system is well documented (**Figure S1**). For instance, Ms for equiatomic $Ni_{50}Ti_{50}$ is approximately 330 K, whereas a slight increase in the Ni content to $Ni_{50.3}Ti_{49.7}$ lowers Ms to around 300 K. Consequently, $Ni_{50}Ti_{50}$ and $Ni_{51.2}Ti_{48.8}$ were selected as martensitic and austenitic compositions for this work, respectively, as they are sufficiently distant from any transformation

temperatures at the testing temperature. This material choice minimizes the risk of undesired phase transitions during experimental procedures, while remaining similar enough in composition to attribute the observed property changes primarily to phase-dependent, microstructural differences [1, 9].

Polycrystalline NiTi specimens were synthesized using the arc melting technique on a water-cooled copper hearth previously described by Frenzel et al. [9, 42]. The melting was carried out under an argon atmosphere to prevent oxidation. To achieve optimal chemical homogeneity, each sample was remelted six times. Following solidification, the specimens underwent homogenization annealing at 1223 K for 24 hours in evacuated quartz ampoules and were subsequently quenched in water to suppress the formation of precipitates.

Specimens for electrochemical testing, measurement of thermophysical properties and phase and topology analysis were extracted as 1 mm thick plates with a base area of 1.28 cm^2. The specimens were cut using an Acutom 10-100 by Struers GmbH, followed by grinding and successive mechanical polishing steps. After polishing with 1 µm diamond suspension, the specimens were electrolytically polished in a LectroPol-5 by Struers GmbH using an optimized electrolyte described by Pohl et al. (79% acetic acid and 21% perchloric acid (70–72% $HClO_4$)) for a duration of 45 seconds at 17 °C [42]. The voltage was 10 V for the $Ni_{50}Ti_{50}$ specimen and 18 V for the $Ni_{51.2}Ti_{48.8}$ one. These different voltages stem from preliminary evaluations of the potential curves of each material. The goal of the electrolytical polishing was twofold. First, it eliminated any topology arising from the previous processing (including the martensitic transformation in the $Ni_{50}Ti_{50}$ specimens), and second, it remediated any deformation-induced martensite formation at the surface of the otherwise austenitic $Ni_{51.2}Ti_{48.8}$ specimens (**Figure S2**). The preceding mechanical polishing addressed reproducibility issues arising from variable initial and final surface roughness values [38].

2.2. Characterization

2.2.1. Microstructure Characterization

X-ray diffraction (XRD) was employed for phase analysis in a Bruker D8 Advance diffractometer with a Cu Kα radiation source with a wavelength of 1.5406 Å. The selected 2θ range varied from 30° to 100° with a step size of 0.02° and a dwell time of 10 s. The surface of the sample was scanned through its rotation around its vertical axis. The diffraction spectra were analyzed using the software DIFFRAC.EVA.

A MIRA3 field emission scanning electron microscope (SEM) by Tescan GmbH equipped with a field emission gun was employed to capture micrographs and analytic microstructure information. All investigations were performed with an acceleration voltage of 15 kV and a working distance of 15 mm. Local composition information was captured by energy-dispersive spectroscopy (EDS) through an AZtec Energy Advanced system by Oxford Instruments simultaneously to crystallographic data that was acquired through electron backscatter diffraction (EBSD) using a Nordlys nano detector by Oxford Instruments. Data processing and analysis was performed in the software AZtecCrystal, also by Oxford Instruments.

2.2.2. X-ray Photoelectron Spectroscopy (XPS)

Surface compositions of $Ni_{50}Ti_{50}$ and $Ni_{51.2}Ti_{48.8}$ specimens were determined by XPS. XPS measurements were conducted employing a ULVAC-PHI Versaprobe II, (Chanhassen, USA) device. The NiTi specimens were analyzed applying an Al Kα radiation (hν = 1253.6eV) with a band-pass energy of 11.75eV. As a reference, the XPS spectra were calibrated using the C1s adventitious carbon C–C binding energy at 284.8 eV. All spectra were analyzed with the CasaXPS 2.3.25 software.

2.2.3. Atomic Force Microscopy (AFM)

The surface topography of the $Ni_{50}Ti_{50}$ and $Ni_{51.2}Ti_{48.8}$ specimens, both before and after electrochemistry measurements were characterized using AFM with the TOSCA 400 (Anton Paar Germany GmbH). To statistically back up the results, multistage data quantification (MSDQ) that we recently developed to accurately extract quantitative and representative surface features [43] was applied. The methodologies and conditions followed in this study are consistent with those outlined in our previous work [44], and the specific parameters used are detailed in the supporting information section S1. In addition, combined AFM and conductive AFM (cAFM) measurements for characterization of the local transport properties were performed on a Cypher ES Environmental AFM (Oxford Instruments, Santa Barbara, CA, USA). For the measurements, CDT-NCHR (NANOSENSORS, Neuchatel, Switzerland) AFM tips with boron-doped diamond-coating were used. A bias of 0.5 V was applied to the back electrode through a 500 MΩ resistor.

2.2.4. Thermophysical Properties

Temperature-dependent electrical resistivity measurements were conducted using a closed-cycle cryostat. Electrical contacts were established using an aluminum wire applied via wedge bonding. Measurements were performed using an alternating current of 10 mA, and the signal was amplified and detected employing lock-in technique to amplify the signal [2].

2.2.5. Contact Angle Measurements

Contact angle measurements were performed using OCA15PRO equipment (Data Physics Instruments GmbH). The measurements were conducted using 1 M KOH as the probe liquid which was dropped at a drop-eject-rate of 5 μL s^{-1}.

2.2.6. Beaker Cell Electrochemical Measurements

For the alkaline OER analysis, the electrochemical performance of the specimens was tested by using them as working electrodes in a three-electrode beaker cell setup. A spiral Pt wire was the counter electrode, and Hg/HgO in 1 M KOH was used as the reference electrode. All experiments were performed under ambient condition in 100 mL of 1 M KOH (Pellets, 85%, Sigma Aldrich). A Biologic potentiostat VMP3 (BioLogic, France) was used to control the potential.

The measurement sequence began by recording the open circuit potential (OCP) for 60 seconds to enable the system to reach a stable equilibrium potential. Potentiostatic electrochemical impedance spectroscopy (PEIS) was then performed at OCP over a frequency range of 100 kHz to 10 Hz with 10 mV rms AC voltage to determine the uncompensated resistance (R_u). The real impedance value was obtained where the phase angle reached a minimum and used for potential correction with respect to reversible hydrogen electrode (RHE). Before evaluating the OER, the catalyst underwent electrochemical preconditioning by cycling 50 CVs (Cyclic Voltammograms) between 0.4 and 1.6 V vs. RHE at a scan rate of 100 mV s^{-1} followed by a set of CVs with different scan rates for analysis of the electrochemical active surface area (ECSA). This preconditioning step was essential for stabilizing the catalyst surface and eliminating residual impurities. Subsequently, the OER activity was assessed using linear sweep voltammetry (LSV) at a scan rate of 5 mV s^{-1}.

After conditioning by cyclic voltammetry (CV), electrochemical surface area (ECSA) measurements were carried out. CVs were taken from a potential range (non-faradaic region)

between 1.00 to 1.20 V vs RHE at different scan rates ranging from 20-200 mV s^{-1} to determine the double layer capacitance (CDL) from the current (I) vs. scan rate (U) plot. The slope of the linear fit gives the CDL, which is divided by a constant specific capacitance (Cs), 40 µF/cm^2, giving the ECSA [43]. For current normalization, two approaches were opted, normalization by geometrical cross-sectional area (length × width of the NiTi plate; 1.28 cm^2) and by the electrochemical surface area which is calculated as described above [45]. To study the effect of Fe incorporation during OER, all these experiments were carried out in KOH containing both, 15 and 150 ppb Fe.

3. Results and Discussion

3.1. Microstructure Characterization

As opportunely stated, the core scientific question in this work is based on achieving two different microstructures with comparatively similar NiTi SMA compositions. **Figure 1** shows that, as expected, the $Ni_{51.2}Ti_{48.8}$ specimen presents a diffractogram compatible with a B2 ordered cubic structure (ICDD# 18-0899). The diffractogram of the $Ni_{50}Ti_{50}$, on the other hand, indicates a monoclinic B19' structure (ICDD# 35-0899). This result highlights the success of the material casting and, therefore, the resulting material purity, as no further phases were identified [9]. Furthermore, the absence of martensite in the $Ni_{52.1}Ti_{48.8}$ specimen confirms that the electropolishing step successfully produced deformation-free surfaces [42].

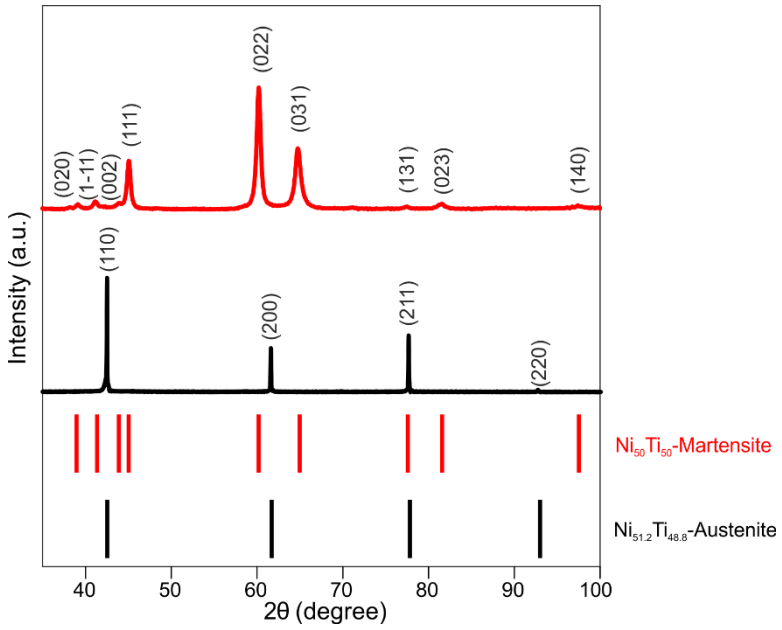

***Figure 1**. XRD diffractogram of the selected alloys after electropolishing. The martensitic $Ni_{50}Ti_{50}$ specimen shows peaks compatible with a B19' structure (ICDD# 35-1281), whereas the austenitic $Ni_{51.2}Ti_{48.8}$ indicates a B2 cubic structure (ICDD# 18-0899).*

The Electron Backscatter Diffraction (EBSD) scans of the electropolished samples provide additional insights into the main features of the microstructures of the studied alloys and their length scales. **Figure 2** presents the inverse pole figure map Y (IPF-Y) a), c), and the phase distributions b), d) of the studied specimens: a,b: $Ni_{50}Ti_{50}$; d,e: $Ni_{51.2}Ti_{48.8}$. The IPF-Y, shows the orientation of the crystallites. As expected from the employed casting and heat treatment process, the grain size of the austenite phase exhibits a coarse grain structure, generally on the order of several hundred micrometres or even reaching to the millimetre range [9, 42]. In the region shown in Figure 2c, the austenite grains extend over 350 µm, whereas the indexed martensite variants shown in Figure 2a have a width ranging between 0.5 and 2 µm. It is worth noting that the $Ni_{50}Ti_{50}$ specimen had a similar austenitic grain size prior to its transformation into martensite, demonstrating the strong microstructural change induced by the displacive phase transition [46, 47]. The EBSD map of $Ni_{50}Ti_{50}$ shows considerable amounts of unindexed positions, represented in Figure 2a,b as dark regions. This incomplete indexing is characteristic of thermally transformed B19' martensite, which self-accommodates to minimize internal lattice strain [3]. This configuration requires the formation of hierarchical nanotwins with lamellar widths that are smaller than the interaction volume of the electron beam, extending down to just a few lattice spacings [48, 49]. Consequently, the EBSD detector captures overlapping Kikuchi patterns from multiple twin variants simultaneously, resulting in pattern interference, low pattern quality, and null solutions [50]. The phase maps (Figure 2b,d) substantiate the findings of the XRD analysis. Ti_2Ni and TiC inclusions were detected and will be discussed later in the surface characterization section. These were not observable in the XRD patterns likely because of their low content and small size.

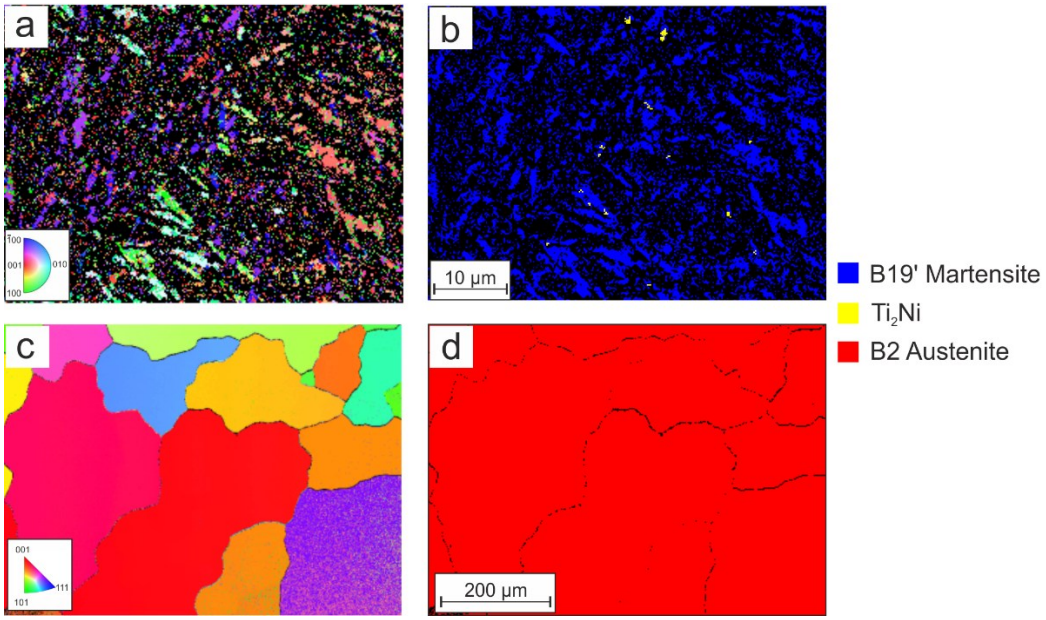

***Figure 2**. EBSD maps of $Ni_{50}Ti_{50}$ a), b); and of $Ni_{51.2}Ti_{48.8}$. c), d). IPF-Y: a), c). Phase map: b), d).*

3.2. Surface Chemical Analysis

To characterize the electropolished surface chemical state of the NiTi specimens prior to electrochemical testing, XPS was performed on both compositions. XPS survey spectra of both NiTi specimens were characterized by the desired elements such as Ni, Ti, O and C as shown in **Figure S3**. These observations are consistent with previous studies, which have shown that the native oxide layer formed on NiTi alloys under ambient conditions is composed primarily of Ti and O, with a lower nickel contribution due to preferential surface oxidation of titanium [51, 52].

High-resolution XPS spectra of Ni 2p (**Figure 3a**) revealed pronounced Ni $2p_{3/2}$ peaks at 852.9 eV and Ni $2p_{1/2}$ peaks at 870.0 eV for both phases. This binding energy is indicative of metallic Ni^0 in these NiTi compositions.

For titanium, the Ti 2p region (Figure 3b) in both martensitic and austenitic alloys displays the characteristic spin-orbit split doublet, with Ti $2p_{3/2}$ at 459.1 eV and Ti $2p_{1/2}$ at 464.8 eV (blue and green deconvoluted peaks), confirming the dominant presence of Ti^{4+} in TiO_2. Lower binding energy components at 457.5 and 456.0 eV (orange/yellow) are attributed to reduced titanium species (Ti^{3+}, Ti^{2+}), and a subtle feature at 454.5 eV is assigned to metallic Ti. These results indicate that the major Ti species belong to Ti^{4+}, however the TiO_2 layer is relatively

thin and graded, allowing detection of both oxidized and metallic titanium, as likewise observed in prior detailed XPS studies [53, 54].

In summary, our XPS measurements reveal that the surfaces of the two as-prepared NiTi electrodes are nearly identical and are dominated by a TiO_2-rich passivating overlayer, with subsurface regions containing both reduced Ti species and mostly metallic Ni. This graded structure is a well-established characteristic of NiTi alloys exposed to air, consistent with titanium's greater oxygen affinity, and it has been directly observed in numerous XPS investigations [51-53, 55].

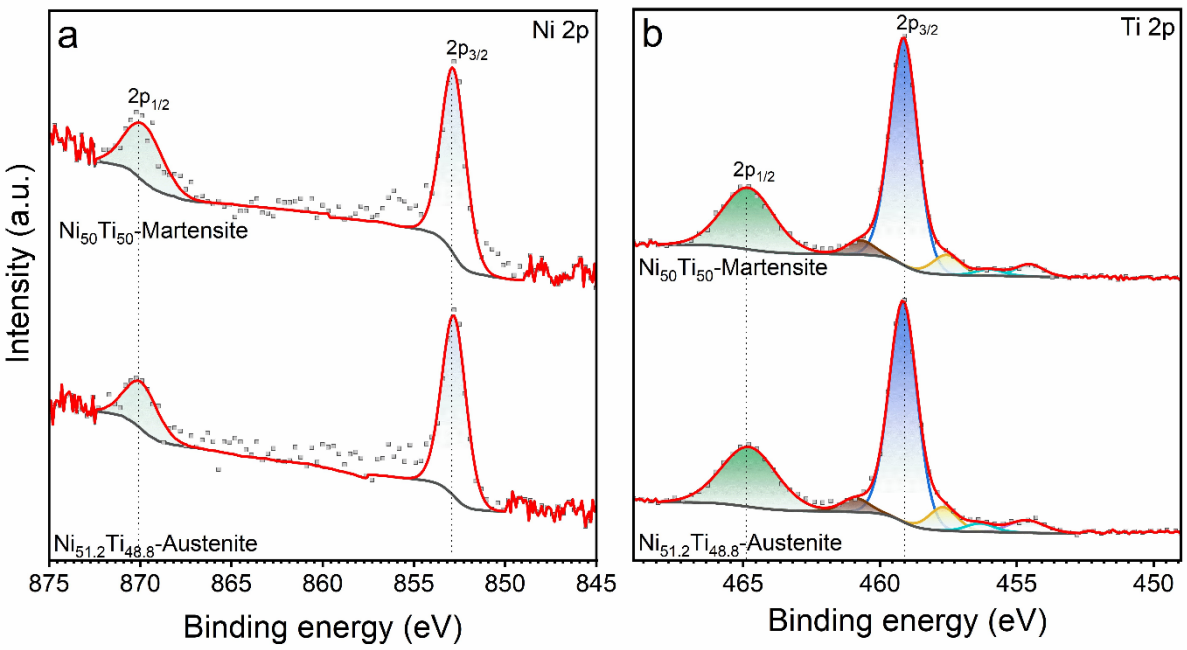

***Figure 3**. High-resolution XPS spectra of Ni 2p (a) and Ti 2p (b) regions for martensitic $Ni_{50}Ti_{50}$ and austenitic $Ni_{51.2}Ti_{48.8}$. The spectra reveal the coexistence of metallic and oxidized states of nickel and titanium, indicating a TiO_2-rich passivating layer with subsurface reduced and metallic species.*

3.3.Surface Morphology Analysis

To evaluate the topography of these NiTi specimens in more detail, SEM and AFM analyses were performed. Together, they reveal the interplay between surface topography and microstructure for the Ni-Ti alloy specimens after electropolishing.

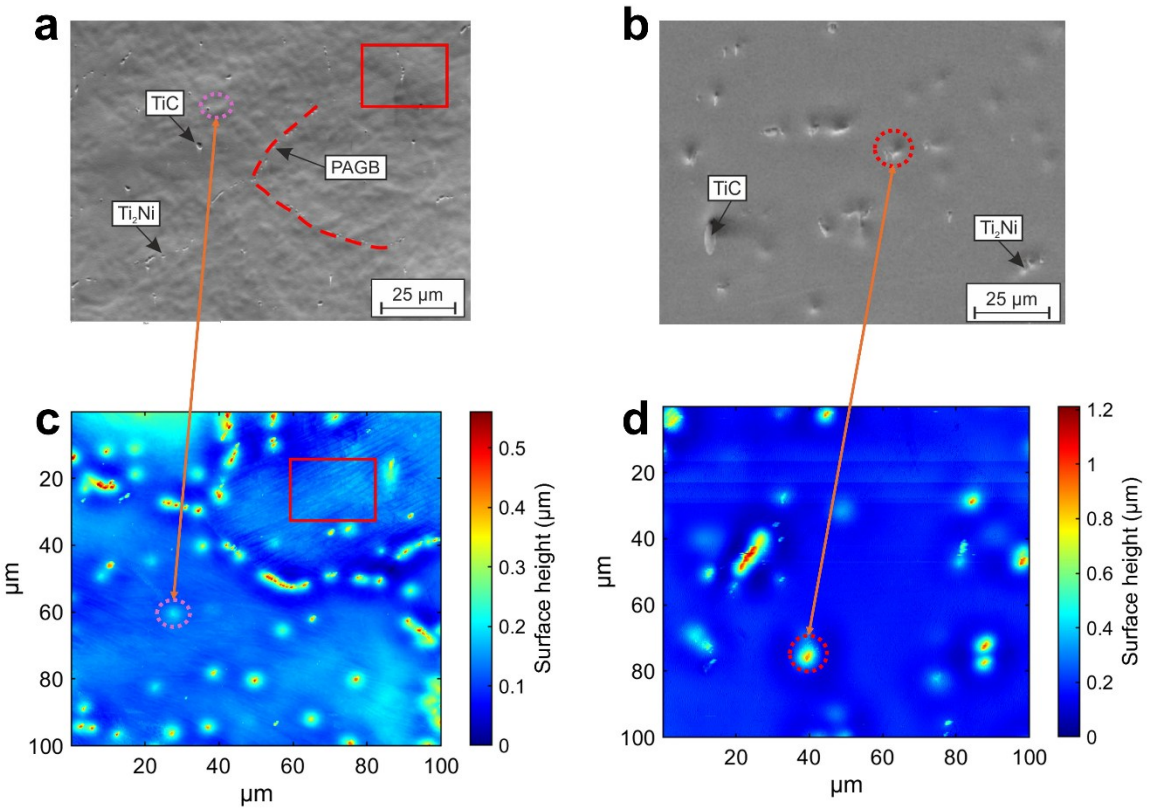

***Figure 4**. SEM and AFM-MSDQ surface analysis of electropolished NiTi SMAs: SEM secondary electron micrographs showing (a) martensitic $Ni_{50}Ti_{50}$ and (b) austenitic $Ni_{51.2}Ti_{48.8}$ surface morphology and impurity distribution and corresponding AFM topographical images of (c) $Ni_{50}Ti_{50}$ and (d) $Ni_{51.2}Ti_{48.8}$ specimens.*

First, SEM investigations provide a microstructural perspective (**Figure 4a,b**). They reveal different surface topographies for the martensitic and austenite specimens. Both exhibit Ti_2Ni and TiC phase-type inclusions (identified via SEM and EDS data, see **Figure S4,** simultaneously captured to the EBSD data shown in Figure 2). These inclusions appear randomly scattered in both specimens, with some occasionally positioned at (prior) austenite grain boundaries (PAGB) (Figure 4a). These phases, which form during solidification by a peritectic reaction in intercellular/interdendritic regions [1] , are related to the purity of the material: The Ti_2Ni phase is stabilized by small amounts of oxygen, which cannot be solved in the NiTi matrix [1]. TiC, on the other hand, is the result of carbon contamination. Besides the inclusions, these SEM micrographs indicate that the prepared specimens exhibit differences in the underlying topography of the phases themselves. When considering the martensite and austenite surface independently from the inclusions, the martensite specimen shows a distinct surface texture that is absent in the austenite one (see the red box in Figure 4a).

Subsequently, AFM was employed and analysed by in-house developed MSDQ that enables a

statistically relevant extrapolation of small-area features to the whole specimen area [43]. Parameters derived in the primary MSDQ stage are given in **Table ST1**. Figure 4c,d show the surface topography of the $Ni_{50}Ti_{50}$ and $Ni_{51.2}Ti_{48.8}$ electropolished specimens, respectively. Evaluating the entire 100 x 100 μm^2 region in the AFM-MSDQ image in Fig. 4c, including all topographic anomalies/impurities, the $Ni_{50}Ti_{50}$ (martensitic) specimen exhibits a lower root mean square roughness of 47 ± 13 nm, a reduced maximum surface height of approximately 0.55 μm, and a homogeneity score of 0.98 ± 0.003. In contrast, the $Ni_{51.2}Ti_{48.8}$ (austenitic) specimen has a higher root mean square roughness of 75 ± 13 nm when evaluated for an area of comparable size and reaches a maximum surface height of 1.2 μm, while exhibiting a homogeneity score of 0.97 ± 0.011 which is slightly lower than martensite. This AFM topographical analysis reveals that both specimens exhibit relatively flat surfaces with surface impurities that appear as bumps in both specimens (marked with pink dashed circles in martensite and with red circles in austenite, also visible in the SEM images). The martensite specimen additionally displays elongated features following a line-like pattern (marked with red square boxes), as also observed in the SEM data.

Additional high-resolution topography measurements recorded in parallel with cAFM conductance maps are presented in **Figure 5**. Figure 5a,b display three-dimensional presentations of the surface topography for martensitic $Ni_{50}Ti_{50}$ and austenitic $Ni_{51.2}Ti_{48.8}$, respectively. Corresponding cAFM scans with overlaying contour lines are presented in Figure 5c,d. The AFM measurements are obtained away from the larger defects seen in Fig. 4 c,d and, hence, allow for an evaluation of the local surface structure, giving arithmetic roughness values (mean absolute deviation from the middle value) of 20.3 nm for martensite (Figure 5a) and 14.6 nm for austenite (Figure 5b). The topography data show that for the martensite, variations in height occur at much shorter length scales than for the austenite, which is rather smooth except for sparsely distributed elevated inclusions. This slightly rougher surface in the $Ni_{50}Ti_{50}$ specimen is attributed to the martensite variants: local electropolishing rates are governed by crystallographic orientation [51, 52]. Consequently, a topography arises from the differential dissolution rates of the variously oriented martensite variants, creating surface relief. The corresponding conductance maps (Figure 5c,d) show only minor variations in local conductance in the order of a few nanoampere. Importantly, as highlighted by the contour lines derived from the AFM data, more pronounced variations in the conductance map consistently correlate with topographical features, which leads to the conclusion that they

originate from changes in the tip-sample contact rather than intrinsic electronic inhomogeneities. Aside from these roughness-related variations in conductance, no substantial differences in the local transport behavior are observed, reflecting homogenous transport properties at the micrometer length scale across both specimens.

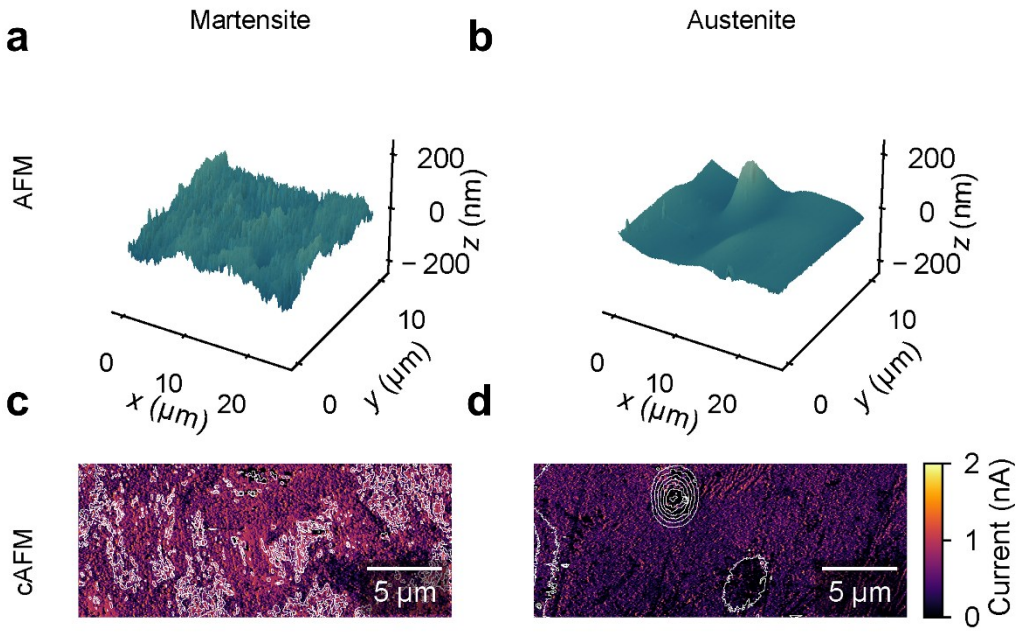

***Figure 5**. AFM-cAFM surface analysis of electropolished NiTi SMAs: Three-dimensional AFM topography of (a) martensitic $Ni_{50}Ti_{50}$ and (b) austenitic $Ni_{51.2}Ti_{48.8}$ anodes, and corresponding (c,d) cAFM current maps with overlaid contour lines, highlighting nanoscale roughness differences and the correlation between local conductance variations and topographical features.*

3.4.Wettability Analysis

Since surface wettability directly influences the electrode-electrolyte interfacial contact and thus the accessibility of active sites during electrochemical reactions, time-dependent contact angle measurements were conducted to investigate the surface characteristics of the NiTi electrode surfaces [56]. A clearly distinct surface wettability between the two NiTi SMA phases was observed. $Ni_{50}Ti_{50}$-martensite exhibited highly hydrophilic behavior with a contact angle of initially 54° which decreases to 21° after 7 sec, while $Ni_{51.2}Ti_{48.8}$-austenite displayed a moderately hydrophilic character with a contact angle of initially 74° that decreases only slightly to 71° after 7 sec. (**Figure 6**). This substantial change in wettability behavior has implications for OER performance, particularly at elevated current densities where oxygen bubble evolution becomes mass-transport-limiting [13, 56]. In particular, hydrophilic surfaces facilitate rapid bubble detachment and efficient gas evolution, preventing bubble accumulation that would otherwise block active sites and increase ohmic resistance [13]. The superior

wettability of the martensite phase also ensures unimpeded access of electrolyte to the catalyst surface and promotes continuous renewal of the electrochemical double layer, thereby sustaining higher catalytic activity [56, 57]. These differences in wettability behavior might originate from the distinct microstructures of the two phases, but they could also result from the slight differences in surface textures observed through SEM and AFM (cf. Figure 3).

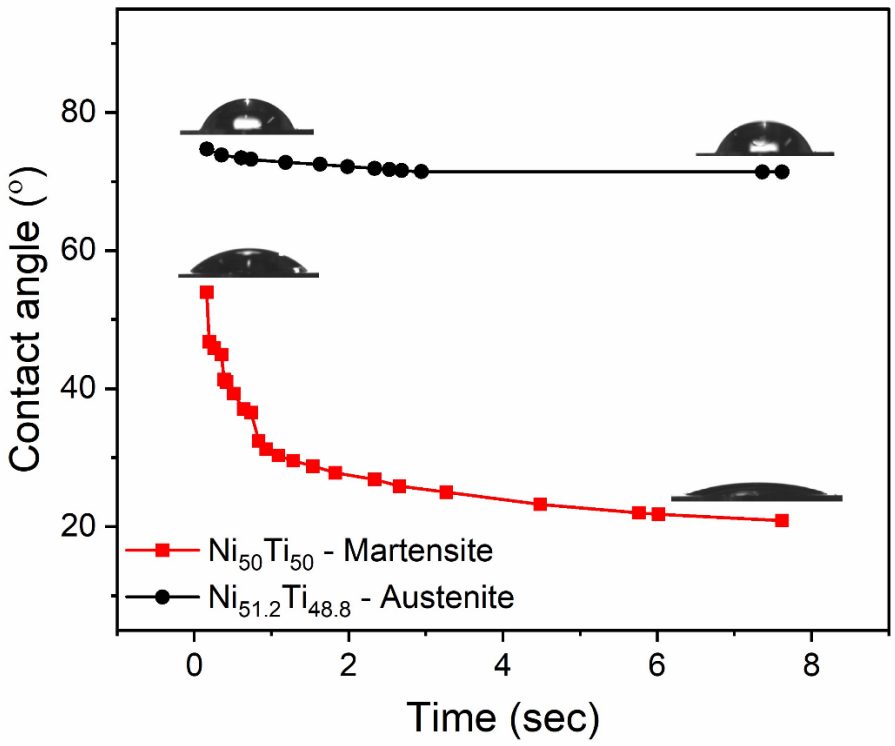

***Figure 6**. Contact angle measurements of (a) $Ni_{50}Ti_{50}$-martensite and (b) $Ni_{51.2}Ti_{48.8}$-austenite specimens, demonstrating the hydrophilic character of the surface. The significantly lower contact angle of the martensite phase indicates enhanced wettability compared to austenite.*

3.5.Electrocatalytic Performance Evaluation

The OER activity of martensitic $Ni_{50}Ti_{50}$ and austenitic $Ni_{51.2}Ti_{48.8}$ was evaluated in 1 M KOH (with 15 ppb Fe) using a standard three-electrode potentiostat configuration. Prior to performance assessment, all electrodes underwent controlled electrochemical conditioning via repetitive cyclic voltammetry (CV) to establish reproducible surface states and minimize contributions from adventitious surface species (see experimental section for details). **Figure 7a** displays the evolution of CVs during the activation protocol. Both compositions exhibited redox features characteristic of the Ni^{2+}/Ni^{3+} couple at approximately 1.4 V vs. RHE, corresponding to the reversible transformation between $Ni(OH)_2$ and NiOOH, the catalytically active Ni-phase for alkaline OER [44]. Notably, the peak characteristics and their evolution over 50 cycles differed markedly between the two compositions.

Following the activation, steady-state polarization curves were recorded via linear sweep voltammetry at a scan rate of 5 mV s^{-1} (Figure 7b). To attain a current density of 10 mA cm^{-2}, $Ni_{50}Ti_{50}$ required an overpotential of 450 mV, representing a 40 mV improvement over $Ni_{51.2}Ti_{48.8}$ (490 mV). This performance difference, while modest in absolute terms, is electrochemically significant given the nearly identical nominal compositions of the two specimens and suggests that variations in microstructure and electronic properties exert measurable influence on the OER performance [58]. The chronopotentiometric (CP) stability test at 10 mA revealed minimal potential drift over 12 hours after an initial performance loss for both electrodes (Figure 7c), with $Ni_{50}Ti_{50}$ operating at 1.56 V and $Ni_{51.2}Ti_{48.8}$ at 1.59 V vs. RHE (at 12 hrs). The absence of significant long-term deactivation indicates that both NiTi intermetallics form more stable oxide/hydroxide surface layers under OER conditions after an initial degradation, limiting further dissolution or passivation [1, 59].

To dissect the underlying mechanisms behind the observed overpotential differences, electrochemical impedance spectroscopy (EIS) was employed. The uncompensated resistance (R_u), measured via potentiostatic EIS, was 0.92 Ω for $Ni_{50}Ti_{50}$ and 1.05 Ω for $Ni_{51.2}Ti_{48}$. While both values are acceptably low, the 14 % reduction in R_u for the martensitic phase further validates the influence of the microstructure in these NiTi SMAs on their electrochemical behavior [60]. The lower uncompensated resistance of $Ni_{50}Ti_{50}$ likely reflects enhanced bulk electronic conductivity in the martensite $Ni_{50}Ti_{50}$ phase. To directly probe bulk transport properties, temperature-dependent electrical resistivity measurements were also conducted (**Figure S5**). At room temperature, the resistivity of martensitic bulk $Ni_{50}Ti_{50}$ was 4.1×10^{-7} Ωm, whereas it was 4.7×10^{-7} Ωm for austenitic $Ni_{51.2}Ti_{48.8}$. These values are consistent with data previously published [2], and closely mirror the trends observed in the EIS measurements. These results confirm distinct charge-carrier characteristics between the two phases, where the martensitic NiTi exhibits higher conductivity in comparison with the austenitic counterpart [2]. The reason behind this behavior is not yet clear. The key might lie in the many interfaces that are created in the displacive phase transformation. Ultimately, because the martensite crystals are small and the twin density is exceptionally high (**Figure 2**), it can be argued that NiTi martensite is an interface-dominated material. Another hypothesis, put forward by Kunzmann et al., proposed that the underlying anomalous electronic behavior is attributable to the potential formation of a Charge Density Wave (CDW) state during the martensitic transformation. While the CDW transition reduces the total free carrier density by locking electrons into bonding orbitals, it simultaneously triggers a drastic increase in carrier mobility, effectively creating a pathway for electron flow [2].

To distinguish the intrinsic activity from the geometrical effect, the electrochemical active surface area (ECSA) was calculated through double layer capacitance in the non-faradaic region (**Figure S6**) [61]. The LSV curves (Figure 7d) were normalized by the ECSA determined from the double layer capacitance. These results align with the trend obtained from the geometric-area normalization, indicating that the observed differences in the activity are correlated to the intrinsic catalytic activity of the specimen. Assuming a specific capacitance of 40 μF cm^{-2} for metal oxide surfaces in alkaline media [61], the ECSA values were determined to be 9.39 cm^2 for $Ni_{50}Ti_{50}$ and 8.41 cm^2 for $Ni_{51.2}Ti_{48.8}$. The higher ECSA of the martensitic phase might be correlated to its slightly higher surface roughness (cf. AFM and SEM data), which, as discussed, likely originated during the electropolishing step itself as a result of the underlying microstructure.

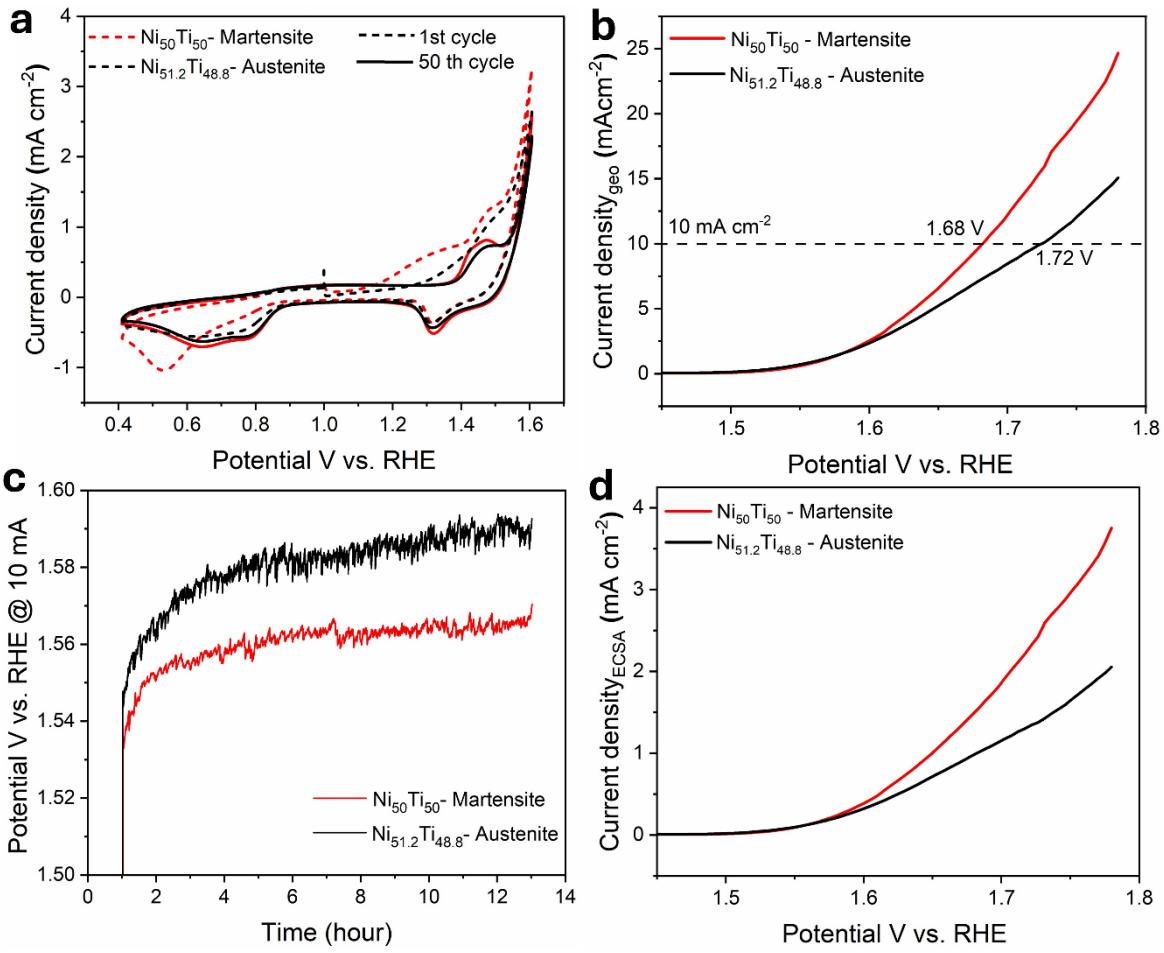

***Figure** 7. Electrochemical characterization and OER performance of austenitic $Ni_{51.2}Ti_{48.8}$ and martensitic $Ni_{50}Ti_{50}$ in 1 M KOH (15 ppb Fe). a) CV conditioning showing the 1st (dashed lines) and 50th cycle (solid lines) at 100 mV s^{-1} in the potential window 0.4–1.6 V vs. RHE. b) LSV for OER activity at 5 mV s^{-1} from geometric-area normalization. c) CP profiles recorded at constant current of 10 mA. d) LSV for OER activity at 5 mV s^{-1} normalized tothe ECSA determined from the double layer capacitance.*

A critical consideration in Ni-based OER electrocatalysis is the effect of trace Fe impurities, which can be incorporated into $Ni(OH)_2$/NiOOH structures to form highly active NiFe catalytic sites [44, 58]. To investigate whether the observed composition-dependent activity trends in NiTi SMAs are also influenced by the Fe contamination, additional electrochemical measurements were conducted in KOH electrolyte containing 150 ppb Fe. **Figure S7a** depicts the CVs of $Ni_{50}Ti_{50}$ and $Ni_{51.2}Ti_{48.8}$ electrodes in 150 ppb Fe-containing electrolyte during the electrochemical conditioning over 50 cycles where these specimens presented different surface evolution behaviors. The martensitic $Ni_{50}Ti_{50}$ electrode exhibited pronounced, sharper redox peaks that intensify substantially over repeated cycling indicating extensive surface restructuring and formation of highly electroactive species [62]. This points toward a facile incorporation of Fe into the evolving oxy-hydroxy layer in the $Ni_{50}Ti_{50}$ composition. In contrast, the austenitic $Ni_{51.2}Ti_{48.8}$ exhibits minimal redox peak evolution over potential cycling suggesting restricted surface restructuring due to Fe intake in comparison to the martensitic phase. To further validate the influence of the electrolyte Fe concentration on the OER performance, LSV measurements were conducted (Figure S7b). While the austenitic $Ni_{51.2}Ti_{48.8}$ achieved a current density of 10 mA cm^{-2} at an overpotential of 544 mV, the martensitic phase showed 378 mV lower overpotential for the same current density thus underlining its enhanced OER performance at elevated Fe concentrations in the electrolyte. Furthermore, the CP measurements indicated a stable OER performance of these electrodes over 12 h at a current of 10 mA (Figure S7c). Altogether, the electrochemical measurements performed at lower and higher Fe concentrations show that the martensitic $Ni_{50}Ti_{50}$ electrode is more prone to the Fe-induced effects in the OER performance in comparison to the austenitic phase. These results suggest that the $Ni_{50}Ti_{50}$ electrodes behave in a similar way to that of other Ni-containing oxides for OER [44]. Here, it is conceivable that the enhanced edge sites, twin boundaries, and defects in the martensitic phase together with its high surface area compared to the austenite phase might provide undercoordinated, easily accessible sites that facilitate enhanced Fe incorporation from the electrolyte during OER [63]. Regarding the general surface evolution during electrochemical testing, post-electrochemical XPS analysis (Figure S8) confirmed that both specimens underwent surface oxidation to form a Ni $(OH)_2$ phase as expected while the chemical state of Ti remained similar with all the lower oxidation states transforming into Ti^{4+}.

Overall, the enhanced OER performance of martensite can be attributed to the following:

1. Enhanced electrolyte wetting: Better electrolyte-electrode contact maximizing wet surface area for ion transport. The improved wettability features of $Ni_{50}Ti_{50}$ can be mainly

correlated to the phase-dependent microstructure which are distinct from the austenitic phase.

2. Improved electronic transport: B19' martensitic specimens exhibited higher bulk electronic conductivity and reduced uncompensated resistance than the austenitic ones. This higher conductivity facilitates more efficient charge transport within the electrode, a behavior potentially arising from the high density of internal interfaces or phase-specific electronic phenomena.
3. Increased electrochemically active surface area: The martensitic phase exhibits ~10% higher ECSA than the austenite phase owing to the higher surface roughness, providing a greater density of accessible active sites for OER.

All these factors contribute simultaneously to enhancing the OER activity of the martensite phase in comparison with the austenite phase and thus the impact of individual factors cannot be decoupled. However, overall, the electrochemical assessment highlights the impact of distinct phase-dependent electrochemical activity of NiTi intermetallic compounds.

4. Conclusions

This study compares the microstructure properties of martensitic ($Ni_{50}Ti_{50}$) and austenitic ($Ni_{51.2}Ti_{48.8}$) SMAs and their subsequent influence on the performance as OER anodes. After confirming the crystal structures of these NiTi SMAs using XRD coupled with analytic electron microscopy and surface chemical state by XPS, the bulk electronic conductivities were evaluated. The B19’ martensitic specimen showed a lower bulk resistivity (4.1×10^{-7} vs. 4.7×10^{-7} Ωm), characterized by reduced uncompensated resistance (0.92 vs. 1.05 Ω). AFM analysis revealed that both the martensitic and austenitic specimens exhibited homogeneous surface morphologies, with the martensitic specimens showing notably higher surface roughness. The martensitic $Ni_{50}Ti_{50}$ was also characterized by dramatically enhanced hydrophilicity (contact angle 21° vs. 71°), a property expected to reduce mass-transport limitations and promote rapid bubble detachment under high-current operation.

Overall, these changes in the microstructure, conductivity and wetting behaviour contributed to distinct performance of these samples as electrodes in OER. Although the two investigated alloys differ by only 1.2 at.% Ni, martensite $Ni_{50}Ti_{50}$ (B19′) clearly outperforms austenite $Ni_{51.2}Ti_{48.8}$ (B2). In 1 M KOH containing 15 ppb Fe (lower Fe concentration), the martensitic electrode requires 40 mV less overpotential to reach 10 mA cm^{-2} and maintains stable operation at 1.56 V vs. RHE for 12 hours. The performance gap remains even after normalizing to the

respective ECSA, confirming that the enhancement arises from intrinsic catalytic properties rather than purely geometrical effects. We also discussed the interface-dominated nature of the NiTi martensite microstructure - or even the formation of a CDW - as possible explanation for this enhanced performance.

Surface characterization by XPS of the pre- and post-catalyst shows that both alloys possess TiO_2-rich passive layers prior to electrochemical testing and transform into mixed $Ni(OH)_2$/NiOOH phases under anodic polarization, with Ti oxidized fully to Ti^{4+}. However, their restructuring behavior diverges in Fe-containing electrolytes. At 150 ppb Fe, the martensitic electrode undergoes markedly stronger activation, as evidenced by the substantial growth of redox features over 50 conditioning cycles, and achieves a 170 mV lower overpotential than the austenitic phase (1.60 V vs. 1.77 V at 10 mA cm^{-2}). These results demonstrate that the martensite $Ni_{50}Ti_{50}$ phase experiences significantly stronger activation especially in higher Fe-containing electrolyte compared to the austenite $Ni_{51.2}Ti_{48.8}$ phase.

In short, this work establishes the phase-dependent microstructure independent of the nominal composition as a powerful lever for tuning electrocatalytic behavior in intermetallic systems. The martensitic B19′ structure combines advantageous electronic transport, uniform surface conductivity, superior wettability, and enhanced Fe incorporation kinetics, collectively boosting OER performance. NiTi SMAs thus offer a promising strategy for fine-tuning their electrocatalytic performance via controlled phase engineering.

Acknowledgement

The authors acknowledge the financial support from the Federal Ministry of Research, Technology and Space (BMFTR project “PrometH2eus”, FKZ 03HY105F). We are also grateful for the support provided by the Mercator Research Center Ruhr (MERCUR.Exzellenz, ‘DIMENSION’ Ex-2021-0034). This work was also funded by the UDE Postdoc Seed Funding. DS acknowledge the Mat4Hy consortium for cooperative support. Open Access funding was facilitated and organized by Projekt DEAL. We extend our thanks to Dr. Ulrich Hagemann from the Interdisciplinary Center for Analytics on the Nanoscale (ICAN) for their valuable assistance. AK would like to thank the glass technology workshop at the University of Duisburg-Essen, especially Raimund Schmidt and Detlef Kühnemann, for melting of the quartz ampoules and their technical advice. AG would like to acknowledge funding by the DFG (412303109). R.H.D. and D.M. acknowledge funding from the European Research Council (ERC) under the European Union’s Horizon 2020 Research and Innovation Program (Grant Agreement No. 863691). JF acknowledges funding by the DFG through project 549600725.

Supporting Information

Supplementary data to this article can be found in the same document or by the author.

Data availability

The data that support the findings of this study are openly available in Zenodo at 10.5281/zenodo.17877493

Declaration of generative AI and AI-assisted technologies in the writing process

During the preparation of this work the authors used the AI Perplexity in order to improve the readability and language of the manuscript. After using this tool/service, the authors reviewed and edited the content as needed and take full responsibility for the content of the published article.

References

1. Frenzel, J., et al., *Influence of Ni on martensitic phase transformations in NiTi shape memory alloys.* Acta Materialia, 2010. **58**(9): p. 3444-3458.
2. Kunzmann, A., et al., *The role of electrons during the martensitic phase transformation in NiTi-based shape memory alloys.* Materials Today Physics, 2022. **24**: p. 100671.
3. Otsuka, K. and X. Ren, *Physical metallurgy of Ti–Ni-based shape memory alloys.* Progress in materials science, 2005. **50**(5): p. 511-678.
4. Zhou, N., et al., *Effect of Ni4Ti3 precipitation on martensitic transformation in Ti–Ni.* Acta Materialia, 2010. **58**(20): p. 6685-6694.
5. Zhu, J., et al., *Influence of Ni4Ti3 precipitation on martensitic transformations in NiTi shape memory alloy: R phase transformation.* Acta materialia, 2021. **207**: p. 116665.
6. Wen, S., et al., *Effect of Ni content on the transformation behavior and mechanical property of NiTi shape memory alloys fabricated by laser powder bed fusion.* Optics & Laser Technology, 2021. **134**: p. 106653.
7. Wu, Z. and J.W. Lawson, *Theoretical investigation of phase transitions in the shape memory alloy NiTi.* Physical Review B, 2022. **106**(14): p. L140102.
8. Mansouri Tehrani, A., et al., *Influencing the martensitic phase transformation in NiTi through point defects.* Journal of Applied Physics, 2015. **118**(1).
9. Frenzel, J., et al., *On the effect of alloy composition on martensite start temperatures and latent heats in Ni–Ti-based shape memory alloys.* Acta Materialia, 2015. **90**: p. 213-231.
10. Babar, P., et al., *Electronic structure engineering for electrochemical water oxidation.* Journal of Materials Chemistry A, 2022. **10**(38): p. 20218-20241.
11. Song, J., et al., *A review on fundamentals for designing oxygen evolution electrocatalysts.* Chemical Society Reviews, 2020. **49**(7): p. 2196-2214.

12. Dotan, H., et al., *Decoupled hydrogen and oxygen evolution by a two-step electrochemical–chemical cycle for efficient overall water splitting.* Nature Energy, 2019. **4**(9): p. 786-795.
13. Jain, A., et al., *A Proof-of-Principle Demonstration: Exploring the Effect of Anode Layer Microstructure on the Alkaline Oxygen Evolution Reaction.* Advanced Functional Materials, 2025. **35**(19): p. 2421352.
14. Chen, F.-Y., et al., *Stability challenges of electrocatalytic oxygen evolution reaction: From mechanistic understanding to reactor design.* Joule, 2021. **5**(7): p. 1704-1731.
15. Verma, A.K., et al., *Robust Oxygen Evolution on Ni-Doped MoO3: Overcoming Activity–Stability Trade-Off in Alkaline Water Splitting.* Chem & Bio Engineering, 2025. **2**(4): p. 241-252.
16. Park, W. and D.Y. Chung, *Activity–Stability Relationships in Oxygen Evolution Reaction.* ACS Materials Au, 2024. **5**(1): p. 1-10.
17. Soni, A., S.K. Maurya, and M. Malviya, *Exploring electrocatalysts for oxygen evolution: A comprehensive comparative review in alkaline and acidic medium.* Journal of Power Sources, 2025. **636**: p. 236571.
18. Wang, B., et al., *Enhancing the oxygen evolution reaction by tuning the electrode–electrolyte interface in nickel-based electrocatalysts.* Communications Chemistry, 2025. **8**(1): p. 109.
19. Walter, C., P.W. Menezes, and M. Driess, *Perspective on intermetallics towards efficient electrocatalytic water-splitting.* Chemical Science, 2021. **12**(25): p. 8603-8631.
20. Antonyshyn, I., et al., *Al2Pt for oxygen evolution in water splitting: a strategy for creating multifunctionality in electrocatalysis.* Angewandte Chemie International Edition, 2020. **59**(38): p. 16770-16776.
21. Rößner, L. and M. Armbrüster, *Electrochemical energy conversion on intermetallic compounds: a review.* ACS Catalysis, 2019. **9**(3): p. 2018-2062.
22. Jin, S., et al., *Precision-Engineered Intermetallic Nanostructured Electrocatalysts for Oxygen and Hydrogen Reactions in Renewable Energy Systems.* Renewables, 2024. **2**(6): p. 376-404.
23. Lu, F., et al., *Structurally Ordered High-Entropy Intermetallics for Electrocatalysis.* Advanced Energy Materials, 2025: p. e03306.
24. Nair, V.S. and R. Nachimuthu, *The role of NiTi shape memory alloys in quality of life improvement through medical advancements: A comprehensive review.* Proceedings of the Institution of Mechanical Engineers, Part H: Journal of Engineering in Medicine, 2022. **236**(7): p. 923-950.
25. Safaei, K., et al., *Additive manufacturing of NiTi shape memory alloy for biomedical applications: review of the LPBF process ecosystem.* Jom, 2021. **73**(12): p. 3771-3786.
26. Tarniţă, D., et al., *Properties and medical applications of shape memory alloys.* Rom J Morphol Embryol, 2009. **50**(1): p. 15-21.
27. Jani, J.M., et al., *A review of shape memory alloy research, applications and opportunities.* Materials & Design (1980-2015), 2014. **56**: p. 1078-1113.
28. Muralidharan, N., et al., *Strain engineering to modify the electrochemistry of energy storage electrodes.* Scientific reports, 2016. **6**(1): p. 1-9.
29. Ghosh, S., et al., *Climbing the Hydrogen Evolution Volcano with a NiTi Shape Memory Alloy.* The Journal of Physical Chemistry Letters, 2024. **15**(4): p. 933-939.
30. Trepanier, C., et al., *Effect of modification of oxide layer on NiTi stent corrosion resistance.* Journal of biomedical materials research, 1998. **43**(4): p. 433-440.
31. Rondelli, G., *Corrosion resistance tests on NiTi shape memory alloy.* Biomaterials, 1996. **17**(20): p. 2003-2008.
32. Wever, D., et al., *Electrochemical and surface characterization of a nickel–titanium alloy.* Biomaterials, 1998. **19**(7-9): p. 761-769.

33. Toker, S., et al., *Evaluation of passive oxide layer formation–biocompatibility relationship in NiTi shape memory alloys: Geometry and body location dependency.* Materials Science and Engineering: C, 2014. **36**: p. 118-129.
34. Vashishtha, H. and J. Jain, *Unraveling the passive film formation and degradation mechanism of NiTi shape memory alloy: An experimental investigation.* Materials Today Communications, 2022. **33**: p. 104734.
35. Liu, M., et al., *Corrosion and passive film characteristics of 3D-printed NiTi shape memory alloys in artificial saliva.* Rare Metals, 2023. **42**(9): p. 3114-3129.
36. Pound, B.G., *Comparison of the Passive Behavior of NiTi and CoNiCrMo in Simulated Physiological Solutions.* Corrosion & Materials Degradation, 2025. **6**(1).
37. Vij, V., et al., *Nickel-based electrocatalysts for energy-related applications: oxygen reduction, oxygen evolution, and hydrogen evolution reactions.* Acs Catalysis, 2017. **7**(10): p. 7196-7225.
38. Qiao, R., et al., *Titanium dioxide induced nickel-iron alloy-based precatalyst towards efficient and durable oxygen evolution reaction.* Journal of Alloys and Compounds, 2024. **1004**: p. 175729.
39. Li, Z., et al., *Titanium oxide supported molybdenum-nickel-iron oxide electrocatalyst for efficient and durable oxygen evolution reaction.* Fuel, 2024. **375**: p. 132509.
40. de la Fuente, B., et al., *Nano-TiO2/TiN Systems for Electrocatalysis: Mapping the Changes in Energy Band Diagram across the Semiconductor| Current Collector Interface and the Study of Effects of TiO2 Electrochemical Reduction Using UV Photoelectron Spectroscopy.* ACS Applied Materials & Interfaces, 2024. **16**(37): p. 49926-49934.
41. Burch, R., *Platinum-tin reforming catalysts: I. The oxidation state of tin and the interaction between platinum and tin.* Journal of Catalysis, 1981. **71**(2): p. 348-359.
42. Pohl, M., C. Heßing, and J. Frenzel, *Electrolytic processing of NiTi shape memory alloys.* Materials Science and Engineering: A, 2004. **378**(1-2): p. 191-199.
43. Jain, A., et al., *From Small-Area Observations to Insight: Surface-Feature-Extrapolation of Anodes for Alkaline Oxygen Evolution Reaction.* ChemCatChem, 2024. **16**(5): p. e202301461.
44. Vinayakumar, V., et al., *Ni-Co-O anodes for the alkaline oxygen evolution reaction: Multistage electrode optimization and plasma-assisted activity enhancement enabled by a coherent workflow.* Chemical Engineering Journal, 2025. **523**: p. 167169.
45. McCrory, C.C., et al., *Benchmarking heterogeneous electrocatalysts for the oxygen evolution reaction.* Journal of the American Chemical Society, 2013. **135**(45): p. 16977-16987.
46. Monu, M.C., et al., *Resultant physical properties of as-built nitinol processed at specific volumetric energy densities and correlation with in-situ melt pool temperatures.* Journal of Materials Research and Technology, 2022. **21**: p. 2757-2777.
47. Grossmann, C., et al., *Processing and property assessment of NiTi and NiTiCu shape memory actuator springs.* Materialwissenschaft Und Werkstofftechnik: Entwicklung, Fertigung, Prüfung, Eigenschaften Und Anwendungen Technischer Werkstoffe, 2008. **39**(8): p. 499-510.
48. Waitz, T., et al., *Size effects on martensitic phase transformations in nanocrystalline NiTi shape memory alloys.* Materials Science and Technology, 2008. **24**(8): p. 934-940.
49. Nishida, M., et al., *Self-accommodation of B19' martensite in Ti–Ni shape memory alloys–Part I. Morphological and crystallographic studies of the variant selection rule.* Philosophical Magazine, 2012. **92**(17): p. 2215-2233.
50. Cayron, C., *What EBSD and TKD tell us about the crystallography of the martensitic B2-B19' transformation in NiTi shape memory alloys.* Crystals, 2020. **10**(7): p. 562.

51. Armitage, D.A. and D.M. Grant, *Characterisation of surface-modified nickel titanium alloys.* Materials Science and Engineering: A, 2003. **349**(1-2): p. 89-97.
52. Chu, C., et al., *XPS and biocompatibility studies of titania film on anodized NiTi shape memory alloy.* Journal of Materials Science: Materials in Medicine, 2009. **20**(1): p. 223-228.
53. Wang, R., et al., *Surface XPS characterization of NiTi shape memory alloy after advanced oxidation processes in UV/H2O2 photocatalytic system.* Applied surface science, 2007. **253**(20): p. 8507-8512.
54. Pequegnat, A., et al., *Surface characterizations of laser modified biomedical grade NiTi shape memory alloys.* Materials Science and Engineering: C, 2015. **50**: p. 367-378.
55. Green, S., D. Grant, and J. Wood, *XPS characterisation of surface modified Ni-Ti shape memory alloy.* Materials Science and Engineering: A, 1997. **224**(1-2): p. 21-26.
56. Jain, A., et al., *Wetting across the Lyophilic–Lyophobic Spectrum: Morphological Tuning of Anode Catalyst Layers for the Alkaline Oxygen Evolution Reaction.* ACS Applied Materials & Interfaces, 2025.
57. Zhao, L., et al., *Electrolyte-wettability issues and challenges of electrode materials in electrochemical energy storage, energy conversion, and beyond.* Advanced Science, 2023. **10**(17): p. 2300283.
58. Trotochaud, L., et al., *Nickel–iron oxyhydroxide oxygen-evolution electrocatalysts: the role of intentional and incidental iron incorporation.* Journal of the American Chemical Society, 2014. **136**(18): p. 6744-6753.
59. Simka, W., et al., *Electropolishing and passivation of NiTi shape memory alloy.* Electrochimica Acta, 2010. **55**(7): p. 2437-2441.
60. Zhang, L., et al., *Study on the corrosion behavior of NiTi shape memory alloys fabricated by electron beam melting.* NPJ Materials Degradation, 2022. **6**(1): p. 79.
61. McCrory, C.C., et al., *Benchmarking hydrogen evolving reaction and oxygen evolving reaction electrocatalysts for solar water splitting devices.* Journal of the American Chemical Society, 2015. **137**(13): p. 4347-4357.
62. Mellsop, S.R., et al., *Structure and transformation of oxy-hydroxide films on Ni anodes below and above the oxygen evolution potential in alkaline electrolytes.* Electrochimica Acta, 2015. **168**: p. 356-364.
63. Ou, Y., et al., *Cooperative Fe sites on transition metal (oxy) hydroxides drive high oxygen evolution activity in base.* Nature Communications, 2023. **14**(1): p. 7688.

We compare martensitic ($Ni_{50}Ti_{50}$) and austenitic ($Ni_{51.2}Ti_{48.8}$) at room temperature NiTi shape memory alloys as oxygen evolution reaction (OER) anodes, demonstrating that phase-dependent microstructure governs electronic conductivity, surface roughness, and wettability. The martensitic phase exhibits intrinsically enhanced OER performance and stronger electrochemical activation, particularly in Fe-containing alkaline electrolytes, highlighting phase engineering as an effective route to tune electrocatalytic activity in intermetallic systems.

Vineetha Vinayakumar[1,2*], Santiago Benito[3*], Aneeta Jose[1], Alexander Kunzmann[4,5], Adarsh Jain[1], Ruben Skjelstad Dragland[7], Mohit Chatwani[1], Blaz Toplak[1], Adithya Aravind[1], Dennis Meier[2,5,6,7], Oluwabi Oluwaseyi[8], Jan Frenzel[8], Sebastian Weber[3], Gabi Schierning[2,4,5], Doris Segets[1,2]

A Proof of Principle for the Phase-Dependent Electrocatalytic Activity of NiTi Shape Memory Alloys for Oxygen Evolution Reaction

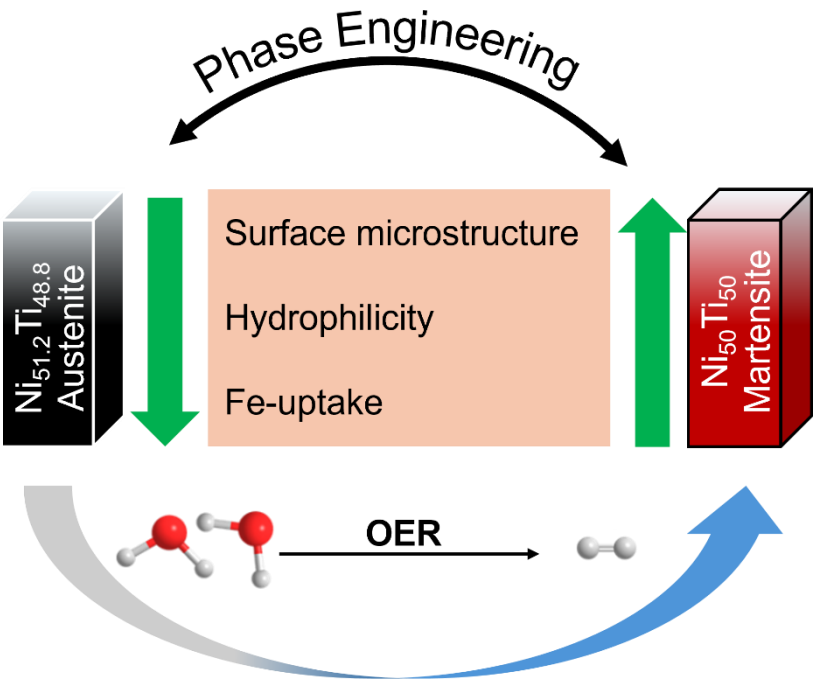

Supporting Information

A Proof of Principle for the Phase-Dependent Electrocatalytic Activity of NiTi Shape Memory Alloys for Oxygen Evolution Reaction

Vineetha Vinayakumar[1,2*], Santiago Benito[3*], Aneeta Jose[1], Alexander Kunzmann[4,5], Adarsh Jain[1], Ruben Skjelstad Dragland[7], Mohit Chatwani[1], Blaz Toplak[1], Adithya Aravind[1], Dennis Meier[2,5,6,7], Oluwabi Oluwaseyi[8], Jan Frenzel[8], Sebastian Weber[3], Gabi Schierning[2,4,5], Doris Segets[1,2]

1. Supplementary Figures, Tables and discussions

1.1 Material Processing

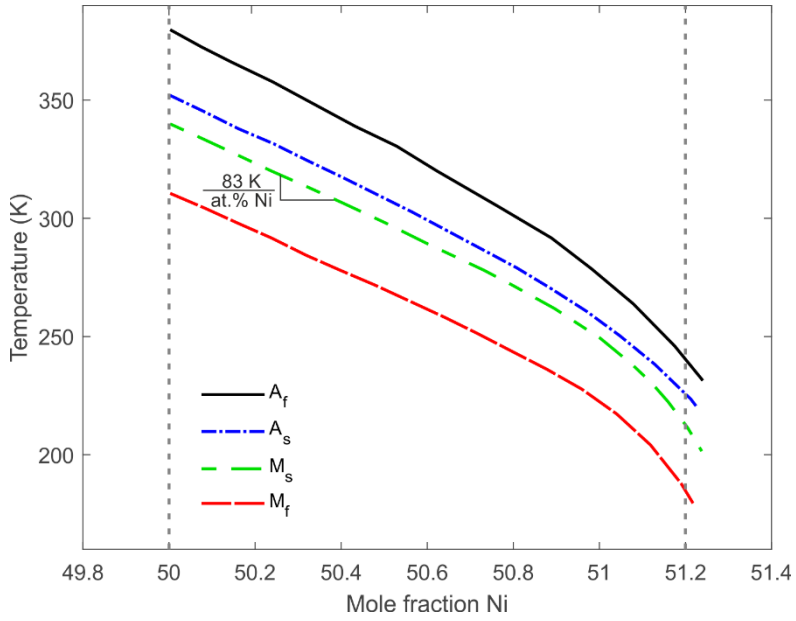

Figure S1. *Dependence of the characteristic temperatures of the martensitic transformation on the nickel concentration in the system Ni_xTi_{100-x} near X=50 at.%. Adapted from [1]. The employed alloys are shown as dashed vertical lines. Upon cooling from austenite: martensite start (Ms) and martensite finish (Mf). Upon heating from martensite: austenite start (As), austenite finish (Af). All temperatures decrease continuously with increasing nickel concentrations. This decrease is initially linear. For instance, for Ms, the slope is of 83 K / at.% Ni. This is followed by a non-linear reduction from nickel contents from approximately 51 at.%.*

1.2 Microstructure characterization

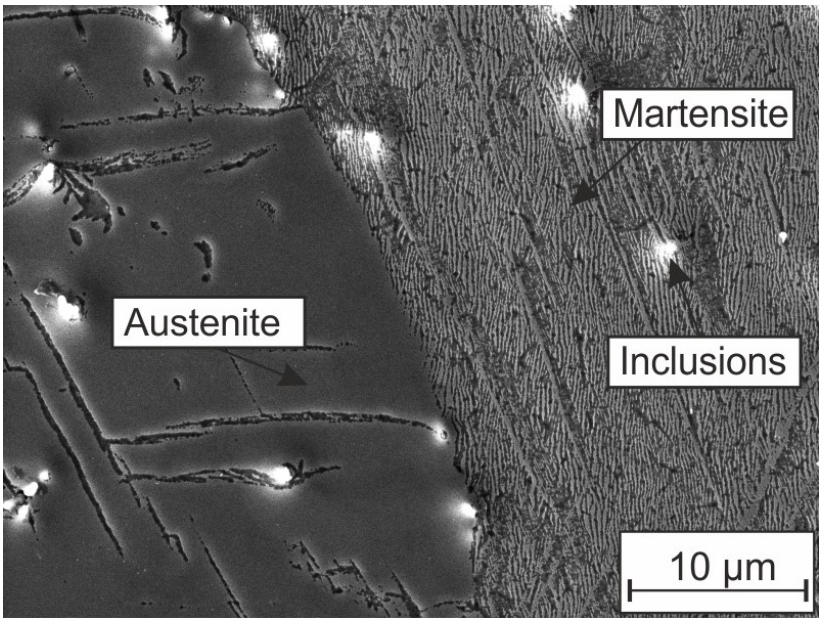

Figure S2. *Deformation-induced martensite formation at the surface of the otherwise austenitic* $Ni_{51.2}Ti_{48.8}$ *specimen caused by mechanical polishing. SEM secondary electron micrograph taken after mechanical polishing and before electropolishing. The electropolishing step is effective at generating deformation-free, smooth surfaces. The topography of the martensitic region stems from the martensitic transformation during polishing itself, coupled with material removal through abrasion.*

1.3 Surface chemical analysis

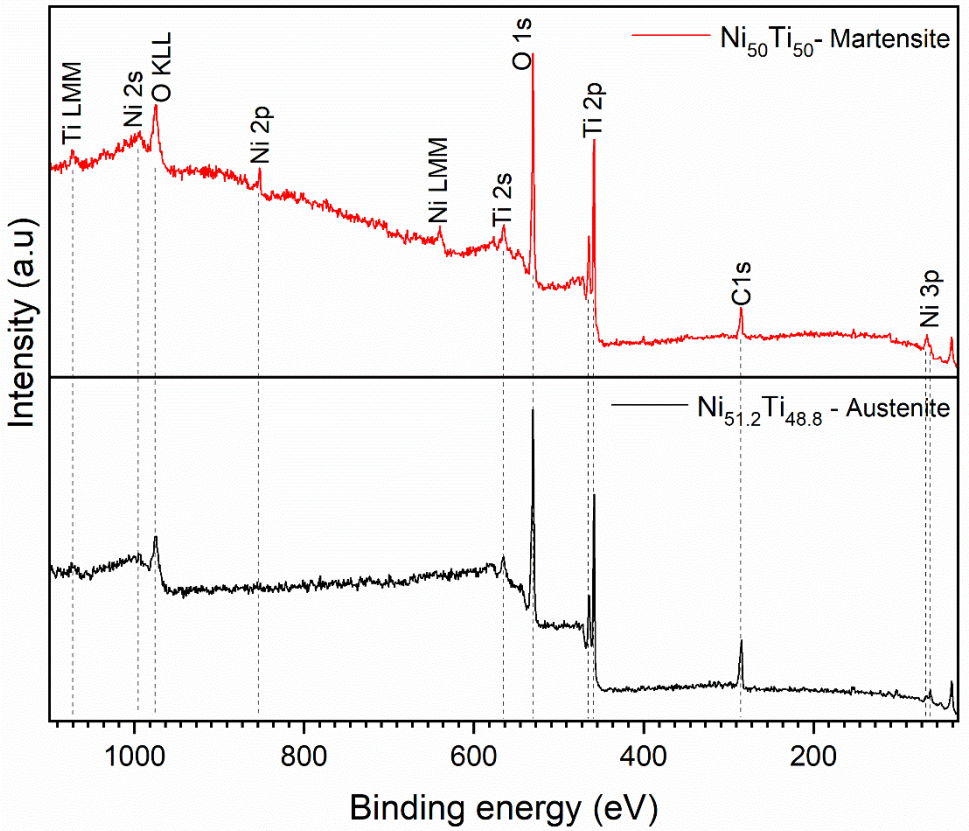

***Figure S3**. XPS survey spectra of both $Ni_{50}Ti_{50}$ -martensite and $Ni_{51.2}Ti_{48.8}$ -austenite with significant elemental peaks marked.*

1.4 Surface Morphology Analysis

Table ST1. Parameters utilized in MSDQ: Homogeneity score (Hs) at different region of selection (ROS), standard deviation (σ), margin of error (E), confidence interval (α) and optimal number of ROS (x) for $Ni_{50}Ti_{50}$ -martensite and $Ni_{51.2}Ti_{48.8}$ -austenite samples.

Parameters	$Ni_{50}Ti_{50}$	$Ni_{51.2}Ti_{48.8}$
$H_{s\,(ROS1)}$ /-	0.98729	0.97162
$H_{s\,(ROS2)}$ /-	0.98598	0.97125
$H_{s\,(ROS3)}$ /-	0.99231	0.97988
$H_{s\,(ROS4)}$ /-	0.98496	0.95344
σ /-	0.003259	0.000668
E /%	5	5
α /%	95%	95%
x_z /-	4	4
x /-	0.98729	0.97162

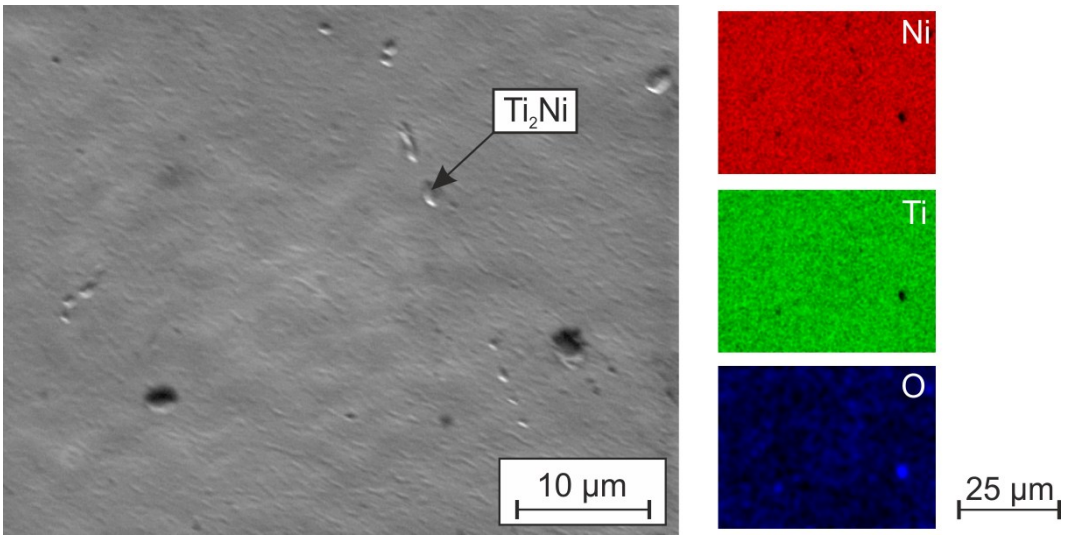

***Figure S4**. Identification of the impurities present in the specimen microstructures. Here exemplarily shown for Ni50Ti50. SEM (secondary electron contrast) and the corresponding composition maps for the elements Ni, Ti, and O.*

1.4. Electrocatalytic Performance Evaluation

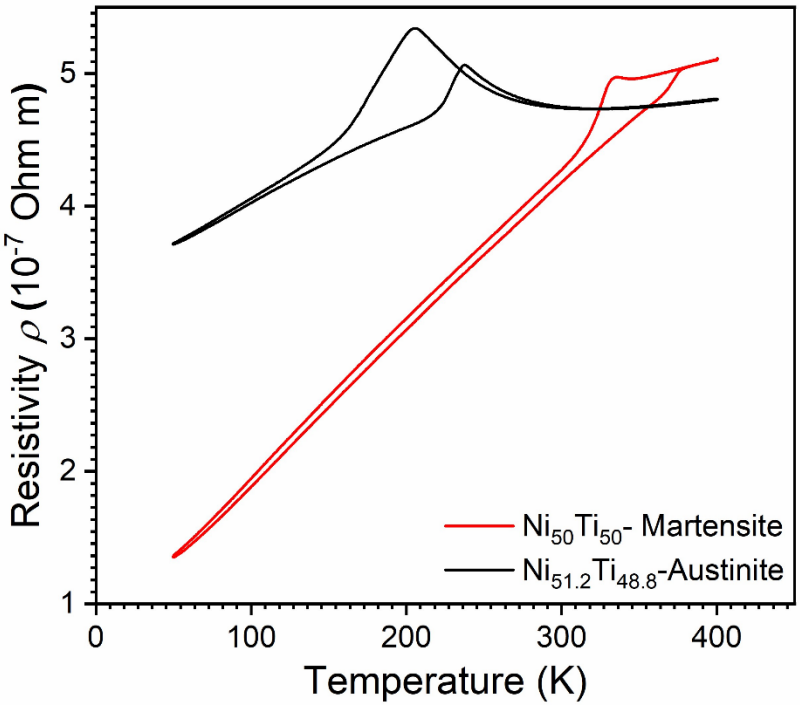

***Figure S5**. Temperature dependent electrical resistivity data, ρ, of the investigated $Ni_{50}Ti_{50}$ - martensite and $Ni_{51.2}Ti_{48.8}$ - austenite specimens [2]*

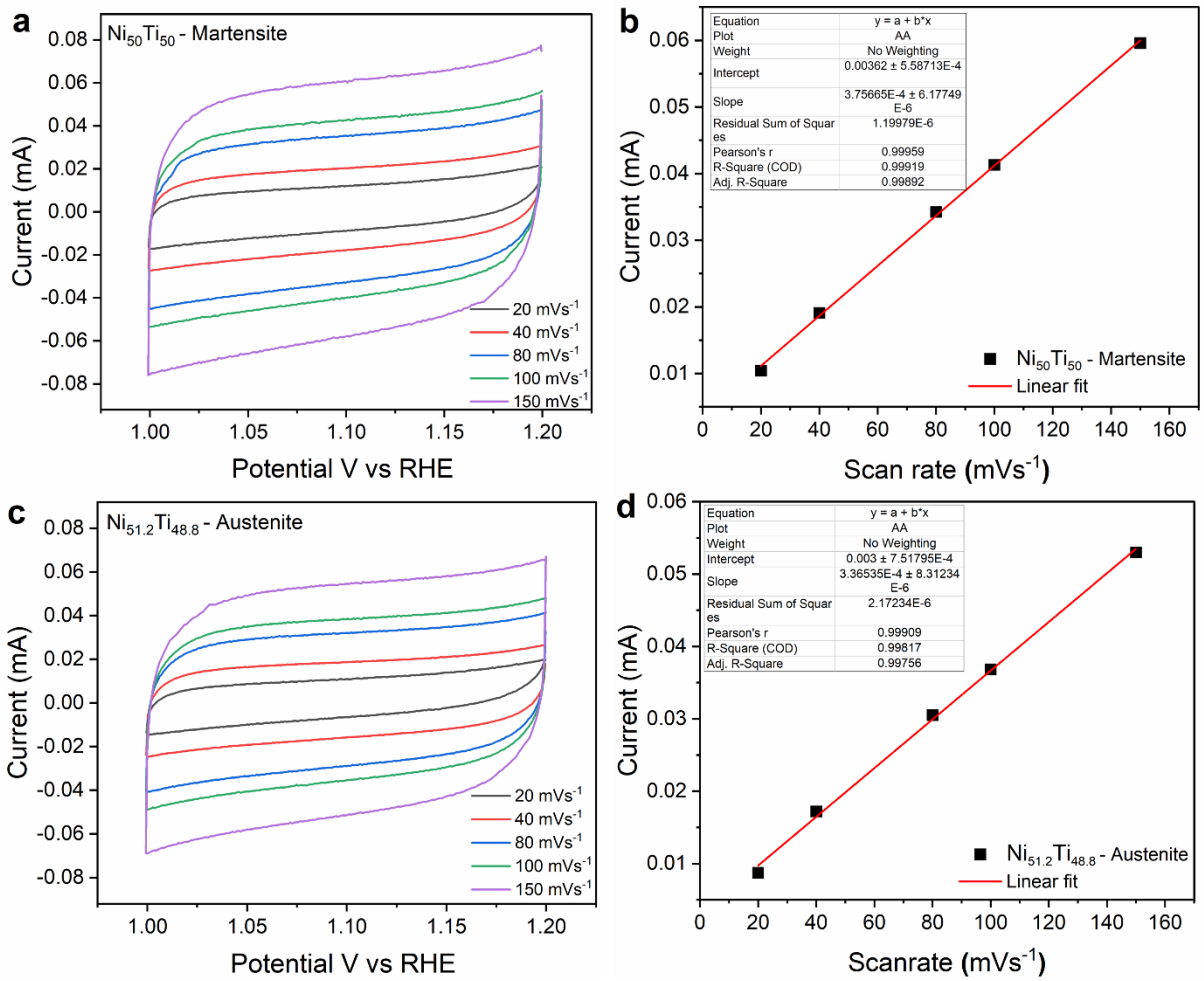

Figure S6. *Electrochemically active surface area (ECSA) determination for $Ni_{50}Ti_{50}$ martensite (a, b) and $Ni_{51.2}Ti_{48.8}$ austenite (c, d) using 15 ppb Fe KOH. (a, c) CV curves at different scan rates (20 to 150 mV s^{-1}) in the non-faradaic region. (b, d) Linear relationship between capacitive current and scan rate, used to calculate the double-layer capacitance (Cdl). The Cdl values are used to calculate the ECSA, with martensite showing a slope of 3.756 × 10^{-4} $A{\cdot}V^{-1}{\cdot}s$ and austenite 3.365 × 10^{-4} $A{\cdot}V^{-1}{\cdot}s$, indicating comparable electrochemically active surface areas.*

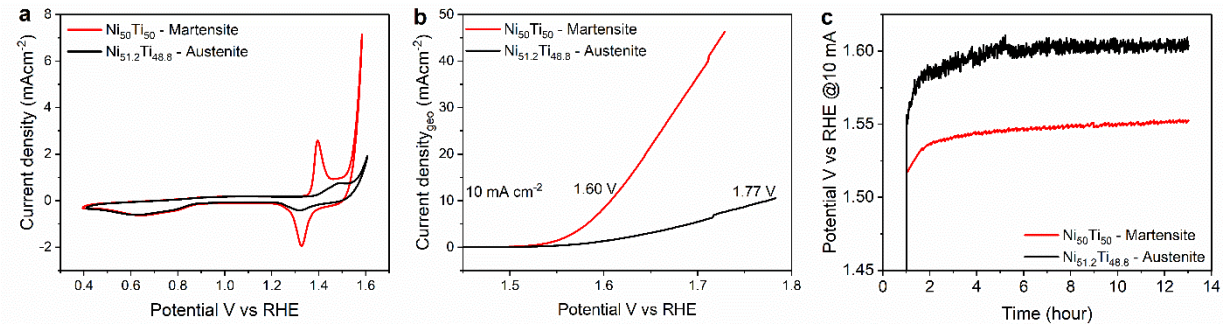

***Figure S7**. (a) CV of $Ni_{50}Ti_{50}$-martensite and $Ni_{51.2}Ti_{48.8}$-austenite showing the 50th cycle measured at 100 mV s^{-1} over 0.4–1.6 V vs. RHE, highlighting distinct phase-dependent redox behavior. (b) CP curves recorded at 10 mA in 1 M KOH with 150 ppb Fe complement the CV analysis.*

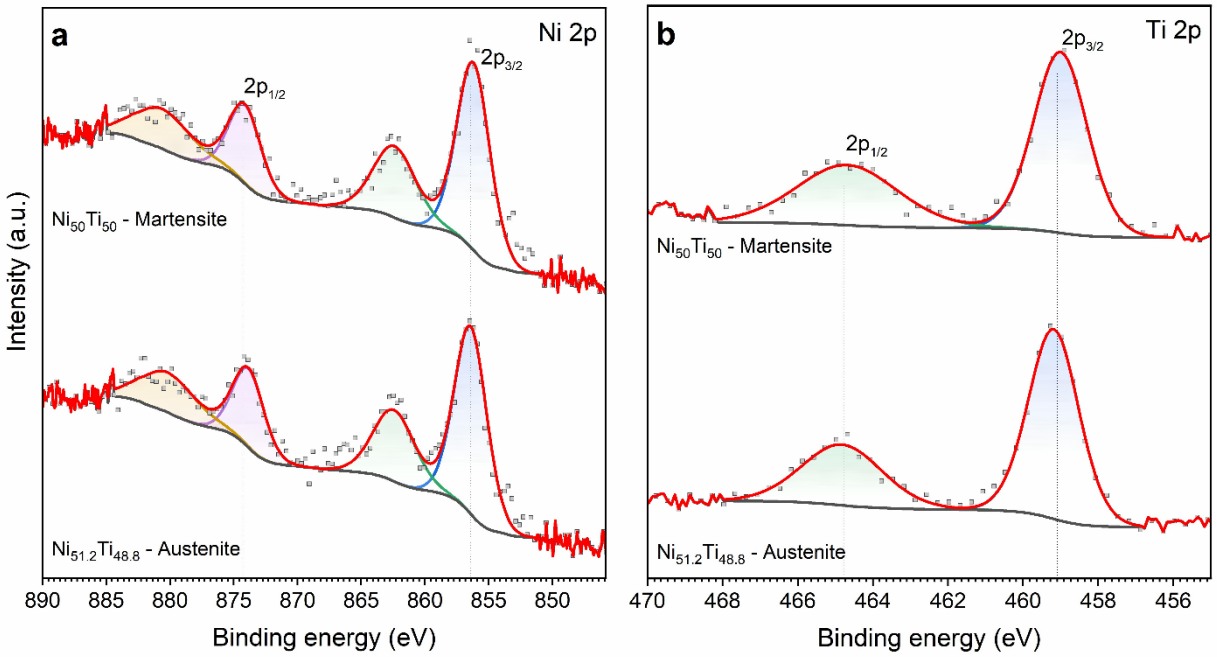

***Figure S8**. High-resolution XPS spectra of Ni 2p (a) and Ti 2p (b) regions for martensite $Ni_{50}Ti_{50}$ and austenite $Ni_{51.2}Ti_{48.8}$. after electrochemistry. The enhanced satellite features in Ni 2p and broadening/shift in Ti 2p spectra indicate formation of $NiO/Ni(OH)_2$ and TiO_2 passive films.*

References

1. Frenzel, J., et al., *Influence of Ni on martensitic phase transformations in NiTi shape memory alloys.* Acta Materialia, 2010. **58**(9): p. 3444-3458.
2. Kunzmann, A., et al., *The role of electrons during the martensitic phase transformation in NiTi-based shape memory alloys.* Materials Today Physics, 2022. **24**: p. 100671.